nature geoscience

ARTICLES

https://doi.org/10.1038/s41561-020-00646-4

Permian–Triassic mass extinction pulses driven by major marine carbon cycle perturbations

Hana Jurikova[1,2,6]✉, Marcus Gutjahr[1], Klaus Wallmann[1], Sascha Flögel[1], Volker Liebetrau[1], Renato Posenato[3], Lucia Angiolini[4], Claudio Garbelli[3], Uwe Brand[5], Michael Wiedenbeck[2] and Anton Eisenhauer[1]

The Permian/Triassic boundary approximately 251.9 million years ago marked the most severe environmental crisis identified in the geological record, which dictated the onwards course for the evolution of life. Magmatism from Siberian Traps is thought to have played an important role, but the causational trigger and its feedbacks are yet to be fully understood. Here we present a new boron-isotope-derived seawater pH record from fossil brachiopod shells deposited on the Tethys shelf that demonstrates a substantial decline in seawater pH coeval with the onset of the mass extinction in the latest Permian. Combined with carbon isotope data, our results are integrated in a geochemical model that resolves the carbon cycle dynamics as well as the ocean redox conditions and nitrogen isotope turnover. We find that the initial ocean acidification was intimately linked to a large pulse of carbon degassing from the Siberian sill intrusions. We unravel the consequences of the greenhouse effect on the marine environment, and show how elevated sea surface temperatures, export production and nutrient input driven by increased rates of chemical weathering gave rise to widespread deoxygenation and sporadic sulfide poisoning of the oceans in the earliest Triassic. Our findings enable us to assemble a consistent biogeochemical reconstruction of the mechanisms that resulted in the largest Phanerozoic mass extinction.

Current lines of evidence point to a rather rapid catastrophe (~61 ± 48 kyr)[1] linked to greenhouse gas emissions from the Siberian Traps large igneous province (LIP)[2–4]. The magmatism apparently induced a lethal combination of a substantial input of relatively light carbon into the atmosphere[4,5], an increase in global sea surface temperature (SST)[6–10], sporadic to widespread anoxia[11–13] or euxinia[14,15] and ocean acidification[16–18]. The exact causes and consequences, however, remain controversial, and a coherent unifying scenario for the environmental evolution over this important interval in Earth's history is still lacking. To reconstruct the carbon cycle dynamics, we generated a new record of ocean pH for the Permian/Triassic boundary (PTB) using boron isotopes (a well-established proxy for ambient seawater pH)[19–23] paired with carbon and oxygen isotope data. Our records were assimilated into a box model, which enabled us to simulate the carbon release and turnover, and study its effects on the Earth's system—a critical exercise to untangle the driving mechanisms of the extinction, as well as to improve our overall understanding of Earth's climatic and ecological sensitivities.

Boron isotope record of Tethys Ocean acidification

We generated high-resolution boron ($\delta^{11}B$), carbon ($\delta^{13}C$) and oxygen ($\delta^{18}O$) isotope records from pristine fossil brachiopod shells[7] composed of low-magnesium calcite (Fig. 1, Methods and Supplementary Information). Our records are based on samples from three stratigraphically well-characterized sections[24] in the Southern Alps of northern Italy—Sass de Putia, Tesero and Val Brutta—where the comparatively uncondensed sedimentary sequences enable a chronologically well-resolved exploration of Tethys Ocean conditions at the PTB (Fig. 1a). This interval covers the global negative carbon isotope excursion (CIE), a characteristic feature of the PTB, associated with major biotic and environmental changes. In addition, several brachiopod specimens from a distant Shangsi section in South China[18] were analysed for comparison. Owing to limited sample availability, the Shangsi record does not overlap with that from the Southern Alps, so a precise stratigraphic correlation at such a high-resolution between the two sites is rather complicated. Nevertheless, the critical decline in $\delta^{11}B$ values, as well as in $\delta^{13}C$ and $\delta^{18}O$ values, after the CIE is registered by brachiopod shells from both South China and Southern Alps, lending strong support to our records and that these are representative of Tethys-wide conditions.

The preservation of the original chemical signals in the samples and potential influences from matrix contamination were thoroughly inspected using a wide suite of prescreening routines, which included minor and trace element analyses (Methods, Extended Data Fig. 1 and Supplementary Information). The latter showed that the composition of our samples is broadly consistent with those expected for modern brachiopod species. In several samples though, increased Al/Ca values were detected that are not compatible with primary Al incorporation into the crystal lattice, and may be indicative of sample contamination from clay sediments from the enclosing matrix. These high Al/Ca values, however, did not translate into systematically enriched B/Ca or reduced $\delta^{11}B$; the general trend in our $\delta^{11}B$ record can be reconstructed solely from samples with low Al/Ca values (Extended Data Fig. 2). In addition, the integrity of our $\delta^{11}B$ compositions was cross-checked by combining solution-based and secondary ion mass spectrometry (SIMS) analyses on selected key specimens. The in situ nature of the SIMS

[1]GEOMAR Helmholtz-Zentrum für Ozeanforschung Kiel, Kiel, Germany. [2]Helmholtz Zentrum Potsdam, Deutsches GeoForschungsZentrum GFZ, Potsdam, Germany. [3]Dipartimento di Fisica e Scienze della Terra, Università di Ferrara, Ferrara, Italy. [4]Dipartimento di Scienze della Terra, Università di Milano, Milan, Italy. [5]Department of Earth Sciences, Brock University, St Catharines, Ontario, Canada. [6]Present address: School of Earth and Environmental Sciences, University of St Andrews, St Andrews, UK. ✉e-mail: hj43@st-andrews.ac.uk

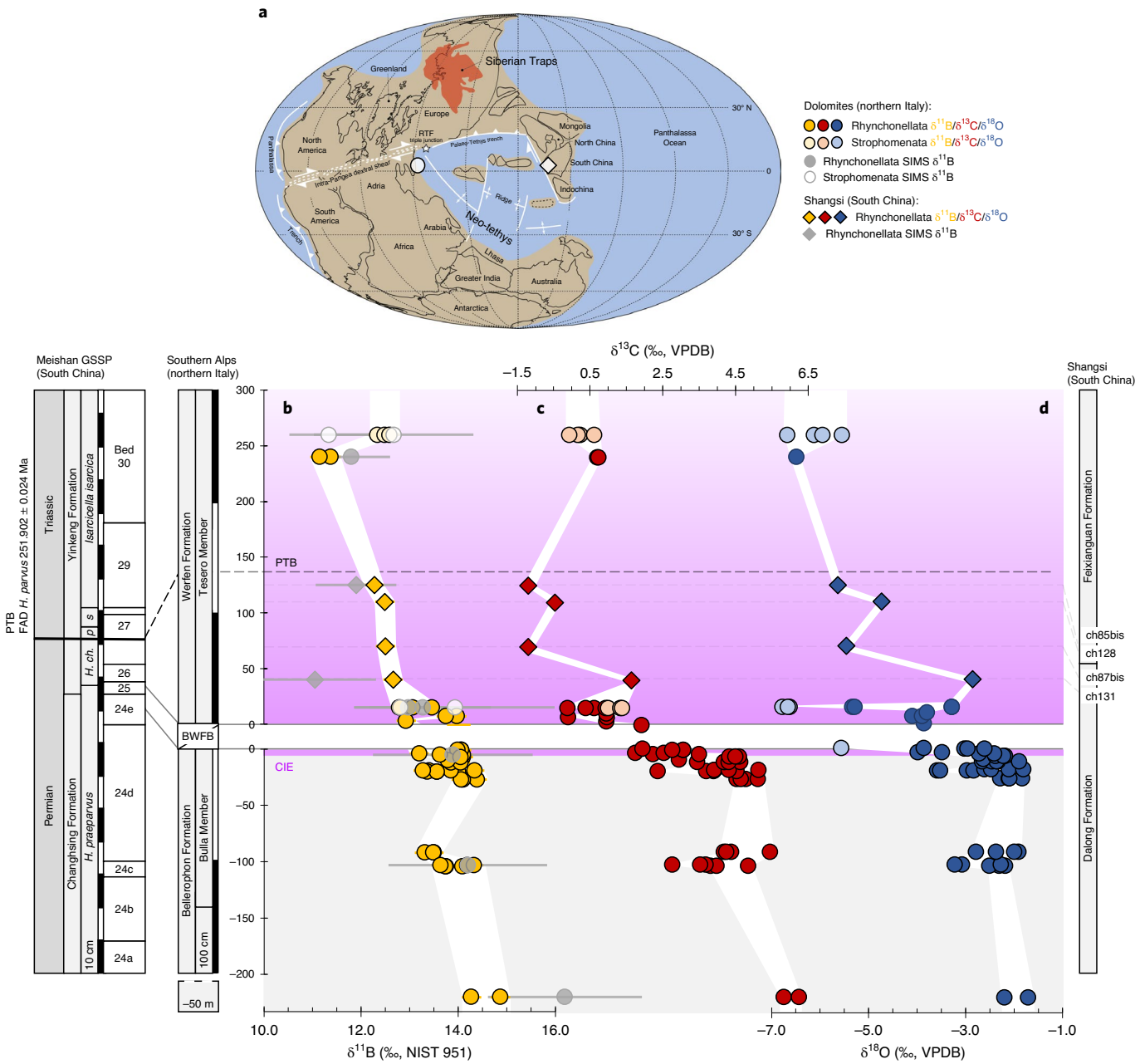

Fig. 1 | Brachiopod-based stable isotope data from Italy and China. a, Late Permian palaeogeographic reconstruction (Methods) with the locations of the sampling sites. **b**–**d**, $\delta^{11}B$ (**b**), $\delta^{13}C$ (**c**) and $\delta^{18}O$ (**d**) records derived from brachiopod shells from Southern Alps (Sass de Putia, Tesero and Val Brutta) and South China (Shangsi). The error bars in **b** indicate the analytical uncertainty for solution-based $\delta^{11}B$ (2 s.d. = 0.2‰) and the s.d. between multiple ion spots measurements within a single shell for SIMS $\delta^{11}B$. The stratigraphy of the Meishan Global Boundary Stratotype Section and Point (GSSP) is shown for comparison. The purple field marks the onset of the CIE as defined in our age model (Methods and Supplementary Information), with the geochronology based on the latest age estimates[1]. Conodont zones: *Hindeodus praeparvus*, *H. changxingensis*, *H. parvus*, *Isarcicella staeschei* and *I. isarcica*. BWFB, Bellerophon–Werfen Formation boundary; FAD, first appearance datum; Ma, million years ago; NIST, National Institute of Standards and Technology; VPDB, Vienna Pee Dee Belemnite; RTF, ridge trench fault.

approach allowed for direct $\delta^{11}B$ measurements within specific shell structures, which provided further supporting evidence that our $\delta^{11}B$ record was not significantly affected by secondary impurities or postdepositional alterations.

The CIE in the Southern Alps in excess of −4.5‰ (Fig. 1c) was accompanied by a decrease in $\delta^{11}B$ values of more than −1.5‰ (Fig. 1b) within some 20 kyr of the latest Permian (Extended Data Fig. 3). This is also closely reflected by a declining $\delta^{18}O$ trend (Fig. 1d), which suggests a dramatic increase in seawater temperatures. Following the CIE, comparably low $\delta^{11}B$, $\delta^{13}C$ and $\delta^{18}O$ values were also found in South China (Fig. 1). We did not observe a recovery to pre-event isotope values after the boundary and into the earliest Triassic. Given the pH-dependent incorporation of $\delta^{11}B$ signal into biogenic calcite, a substantial suppression of ocean pH that accompanies the CIE is evident from our $\delta^{11}B$ data alone. For a quantitative estimate, we converted the $\delta^{11}B$ record to pH given different $\delta^{11}B$-to-pH relationships and ambient seawater $\delta^{11}B$ ($\delta^{11}B_{sw}$) scenarios (Methods). Our preferred scenario accounts for biological

'vital effects' on the incorporation of boron into brachiopod calcite; however, in addition we also considered an alternative scenario based on an aqueous borate ion relationship (Extended Data Fig. 3). The first scenario (hereafter 'standard case scenario') assumes that the $\delta^{11}B$–pH dependency of brachiopod shells is influenced by their internal regulating processes, while the second scenario (hereafter 'borate ion scenario') considers boron incorporation following the inorganic $\delta^{11}B$–pH relationship, hence the lack of vital effects. These two scenarios effectively envelop the plausible $\delta^{11}B$–pH relationships of brachiopod shells[23]. Had ancient brachiopods potentially higher degrees of vital effects, the $\delta^{11}B$ drop in our record would probably translate into an even more extreme acidification scenario, due to the stronger internal pH regulation and resulting dampened sensitivity to the ambient seawater pH. The calibration choice is detailed in Methods and further discussion of the vital effects, which includes a pH and model reconstruction that considers the alternative borate ion scenario, is available in the Supplementary Information. We anchored our initial, pre-CIE $\delta^{11}B$-derived surface ocean pH to plausible pre-event conditions based on previous estimates and our model output. Our $\delta^{11}B$ record then predicted the timing and magnitude of pH fluctuation with respect to the unperturbed starting conditions prior to the mass extinction event. We found a considerable drop of ~0.5 units in ocean pH at the onset of the extinction in the latest Permian that persists into the earliest Triassic (Fig. 2c).

Carbon release impact on redox and nutrient feedbacks

To characterize the associated carbon release and its impact on the environment, we assimilated the carbon isotope and pH data into a geochemical box model (Methods and Extended Data Figs. 4 and 5). The magnitude, dynamics and the most realistic time-resolved $\delta^{13}C$ composition of emitted CO_2 over the PTB was estimated by fitting the model to the data. In addition to our brachiopod data, we considered numerous PTB $\delta^{13}C$ bulk carbonate ($\delta^{13}C_{carb}$; Fig. 2d) and organic carbon ($\delta^{13}C_{org}$; Fig. 2f) isotope records, which comprised different geographical locations and CIE magnitudes, and thereby assured global representation. Our resulting degassing flux (Fig. 2a) amounts to ~$8{,}800 \times 10^{15}$ mol CO_2 (105,600 Pg C, petagram = 1×10^{15} g, equivalent to Gt, gigatonne) over the modelled duration of 1 Myr (−500 to 500 kyr relative to the CIE). A total amount of ~800×10^{15} mol CO_2 (9,600 Pg C) with a mantle signature (−6‰) was initially released until −35 kyr before the CIE. Subsequently, the model diagnoses the emission of ~$8{,}000 \times 10^{15}$ mol CO_2 (96,000 Pg C) of isotopically substantially lighter CO_2 (−18‰). These low $\delta^{13}C$ values reflect the metamorphic degassing of organic carbon during volcanic intrusions into coal basin sediments and are required to match our pH and $\delta^{13}C$ constraints (Fig. 2b). Our outlined emission scenario explains the CIE excursion without invoking a light $\delta^{13}C$ signal from methane clathrates. The LIP carbon budget implied by our model is also broadly consistent with other independent estimates and field data[2–4] (Supplementary Information). Interestingly, the emitted $\delta^{13}C$ signatures and their temporal resolution are also similar to volcanic degassing processes from the North Atlantic Igneous Province during the Palaeocene–Eocene Thermal Maximum[21] some 56 million years ago, although the involved carbon budget for the PTB is nearly an order of magnitude greater (105,600 Pg C as opposed to 12,200 Pg C during the Palaeocene–Eocene Thermal Maximum).

Using a new redox-resolving ocean model[25], we determined the ensuing series of changes in the ocean chemistry (Figs. 2 and 3). In the model, we found that degassing from the Siberian Traps leads to a steep increase in the atmospheric partial pressure of CO_2 (p_{CO_2}), even though a large fraction of the emitted CO_2 is dissolved in the surface ocean, transferred into depth via a gradual increase in export production, and rapidly consumed and converted into bicarbonate via enhanced silicate and carbonate weathering (Fig. 2). Initially,

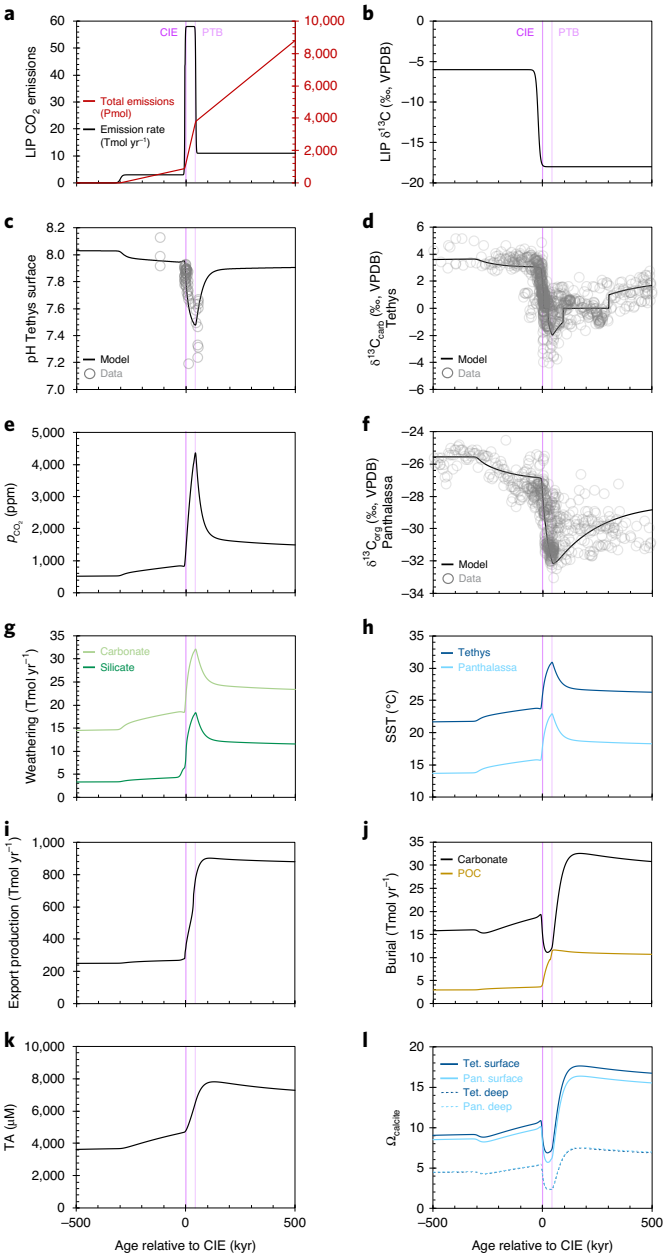

Fig. 2 | Modelled marine carbonate system and climate change. a, CO_2 release via Siberian Traps LIP degassing applied as the model forcing. **b**, Isotopic composition of released CO_2. **c**, Surface pH of Tethys Ocean. **d**, Carbon isotope composition of carbonates deposited on the Tethys shelf (data sources in the Supplementary Information). **e**, Global atmospheric p_{CO_2} projected by the carbon cycle model. **f**, Carbon isotope composition of organic carbon in sediments deposited on the Panthalassa seafloor (data sources in Supplementary Information). **g**, Global rate of silicate (granite + basalt) and carbonate weathering. **h**, SSTs for the Tethys Ocean and Panthalassa. **i**, Marine export production of particulate organic carbon (POC) across a 100 m water depth. **j**, Burial of POC and neritic carbonate on the global shelf. **k**, Seawater total alkalinity (TA). **l**, Saturation state of the surface (0–100 m) and deep waters (>1,300 m) of the Tethys Ocean (Tet) and Panthalassa (Pan) with respect to calcite.

the atmospheric p_{CO_2} is relatively low in the Late Permian (~500 to ~800 ppm, sensu stricto vppm; Fig. 2e). Following the CIE, at the onset of the extinction, CO_2 levels rise abruptly to peak at 44 kyr after the CIE (up to a maximum of 4,400 ppm) and remain elevated

(~1,500 ppm) throughout the Early Triassic, consistent with previous palaeo p_{CO_2} estimates[5,26–29]. The sharp increase in CO_2 imposes a lasting disruption to the marine carbonate cycle, which prompts a severe decline in surface ocean pH (Fig. 2c), which only partially recovers during the Early Triassic. In response to the carbon emission, our model predicts warming by almost 10 °C (Fig. 2h), in agreement with proxy-based evidence[6,30,31]. Rates of chemical weathering strongly increase (Fig. 2g), as does the marine export production (Fig. 2i) and nutrient input, which is congruent with the increase in detrital fluxes to the global ocean observed in numerous sedimentary PTB records[32].

Dissolved oxygen concentrations (Fig. 3a) in subsurface waters decline abruptly soon after the CIE and remain low over the Early Triassic due to the increase in export production and respiration. The surface ocean remains oxygenated through exchange with the atmosphere. Dissolved nitrate (Fig. 3b) sharply increases with the CIE, promoted by a rise in sea surface temperatures (SSTs) and temperature-dependent nitrogen fixation, but it declines again with a coeval increase in pelagic and benthic denitrification brought on by the spread of low-oxygen conditions. Complete depletion of oxygen and nitrate is only attained in the intermediate waters of the Tethys Ocean, where it results in an accumulation of dissolved sulfide (Fig. 2f). Under the post-PTB low-oxygen conditions, ammonium (Fig. 3c), phosphate (Fig. 3d) and iron (Fig. 3e) are released from seabed sediments into the overlying water column and support the rise in export production and respiration in a strong positive feedback loop.

We further extended our model to simulate the turnover of stable nitrogen isotopes ($\delta^{15}N$; Supplementary Information), which reflect the composition of marine organic matter formed in the surface ocean (Fig. 3h). The initial $\delta^{15}N$ decline following the CIE is linked to a rapid rise in nitrogen fixation, but subsequently $\delta^{15}N$ increases due to pelagic denitrification that consumes a large portion of the dissolved nitrate pool in subsurface waters, preferentially removing the light isotope (Fig. 3g). After the consumption of the excess nitrate, $\delta^{15}N$ declines again as a result of ongoing nitrogen fixation. Owing to the strong denitrification under low-oxygen conditions, the modelled plankton growth is largely limited by nitrate, whereas nitrogen fixation is limited by phosphate. Although we acknowledge that the $\delta^{15}N$ model fit, in particular close to the PTB, is less reliable due to the large scatter in the data, the modelled changes explain the overall low $\delta^{15}N$ values in the Early Triassic relative to the Late Permian, a feature reported from numerous sedimentary records[33,34]. This advocates for high SSTs and an increase in the riverine phosphate flux to the ocean induced by enhanced weathering and erosion as triggers of the observed rise in nitrogen fixation and productivity after the PTB.

The increase in global productivity along with the depletion of dissolved oxygen simulated by our redox-resolving model is consistent with data-based reconstructions. Accumulation rates of organic carbon and barite determined in numerous sediment cores from the Tethys Ocan and Panthalassa indicate a substantial increase in export production from the latest Permian into the Early Triassic[32,35]. Marine plankton communities underwent drastic restructuring over the PTB with warming and loss of oxygen, which fostered the proliferation of prokaryotic cyanobacteria over eukaryotic algae[35], which is consistent with the increase in nitrogen fixation predicted by the model. The global loss of oxygen across the PTB has been documented by $\delta^{238}U$ and Th/U records from the Tethys Ocean and Panthalassa, which indicates widespread uranium uptake in sediments after the PTB[11–13]. Conditions in which oxygen and nitrate rather than sulfate are used as terminal electron acceptors for organic matter degradation are also characteristic of modern oxygen minimum zones[36] and lead to uranium accumulation in marine sediments[37]. Evidence for euxinic conditions, in which sulfide dissolved in shallow intermediate waters is transported to the euphotic zone, has been reported from biomarker studies[15].

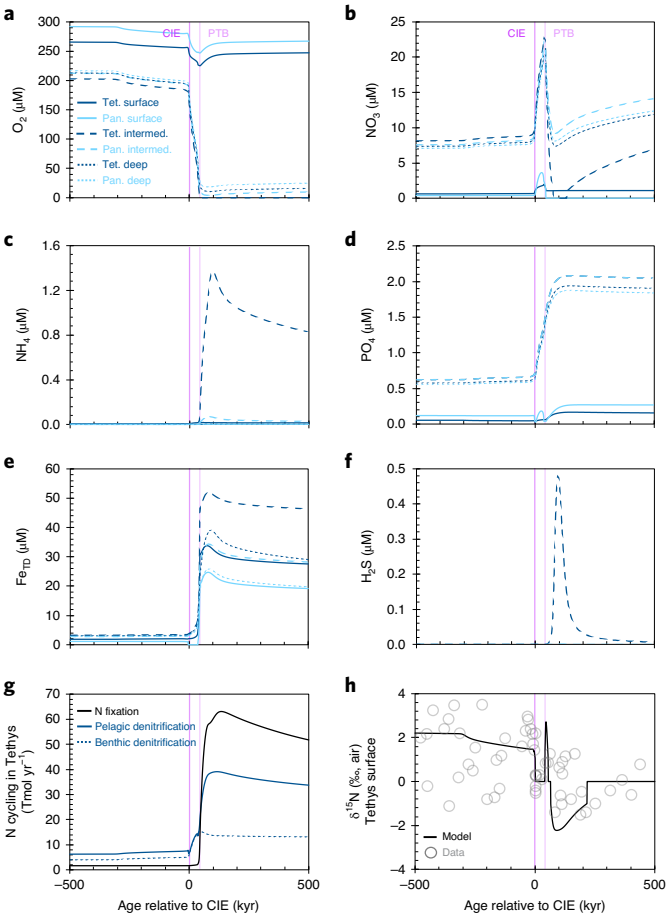

Fig. 3 | Modelled redox state of the ocean, dissolved nutrient concentrations and nitrogen cycling. a–f, Dissolved oxygen (**a**), dissolved nitrate (**b**), dissolved ammonium (**c**), dissolved phosphate (**d**), total dissolved (TD) iron (**e**) and total dissolved sulfide (**f**) in the surface (0–100 m), intermediate (100–1,300 m) and deep waters (>1,300 m) of the Tethys Ocean and Panthalassa. **g**, Reconstruction of nitrogen cycling in the Tethys Ocean. **h**, Nitrogen isotope composition of Tethys sediments (data sources are provided in the Supplementary Information). Intermed., intermediate.

The carbon cycle perturbations culminate at about 100 kyr after the CIE with waning LIP emissions, although neither the atmospheric p_{CO_2} nor the marine biogeochemical cycles return to pre-event conditions during the Early Triassic (Figs. 2 and 3). LIP CO_2 is converted into seawater alkalinity via enhanced chemical weathering. The upsurge of export production aids the drawdown of atmospheric p_{CO_2}, and the ocean pH recovery is additionally augmented by alkalinity production (Fig. 2k) during denitrification under suboxic conditions. Neritic carbonate burial initially declines following the CIE due to a strong acidification of the surface waters, but increases after the PTB in response to an increase in alkalinity (Fig. 2j). As calcifying phytoplankton emerged only later in the Mesozoic, pelagic carbonates were absent during this time and carbonate burial may have only occurred on the shelf. Under such conditions, carbonate compensation would be less efficient than in the modern ocean and could have led to strong calcite oversaturation of the surface waters[38] (Fig. 2l). Our model calculations are also in line with carbonate burial rates derived from strontium and calcium isotope records across the PTB[39,40], and geological evidence of unusually high abiotic calcium carbonate precipitation in the Early Triassic[41]. The marine crisis, however, persists through the Early

Triassic, due to the delayed recovery of the redox state. We note that the evolution of the surface ocean pH and the transition to suboxic conditions is heavily dependent on the initial oxidation state of the ocean, as shown by additional model simulations and sensitivity tests (Supplementary Information). For instance, an increase or decrease of 50% in riverine phosphate input leads to substantial changes in the export production and nitrogen fixation, and thereby the corresponding drawdown of atmospheric p_{CO_2}. Yet, these simulations fail to reproduce the proxy-based evidence, such as the $\delta^{13}C$, pH or $\delta^{15}N$ records, which makes a strong argument in favour of the standard case scenario presented here.

Global consequences for the marine ecosystem

These findings lead us to view the PTB mass extinction as a cascading marine collapse, triggered by a multimillennial-scale voluminous injection of carbon to the atmosphere by the emplacement of Siberian Traps sill intrusions[2,42]. Its magnitude profoundly altered the biogeochemical processes and set off a chain of events that selectively eliminated different groups of marine organisms[43]. In the latest Permian, the CO_2 greenhouse effect resulted in strong heating and acidification of the surface ocean, which prompted the initial disappearance of all reef-building taxa[44,45]. Experiments on modern organisms[46] indicate that an increase in p_{CO_2} alone is generally insufficient to severely impair marine calcification. It is the synergic effect of acidification and rising temperatures that is detrimental, and was presumably lethal to ancient biota. The subsequent extinction pulse followed in the earliest Triassic, with a strong positive redox feedback that drove the deoxygenation of subsurface waters. Both our standard model scenario and further sensitivity tests (Supplementary Information) suggest that the deep ocean remained in a depleted oxygen state, but was not seriously affected by sulfide poisoning. Sulfide formation may have, however, reached toxic levels along the Tethys Ocean's continental margins and in upwelling regions of Panthalassa, where low oxygen and high nutrient concentrations in ascending subsurface waters could have promoted anoxic and/or euxinic conditions, and so aggravated the environmental crisis. The protracted recovery from suboxic conditions and nitrate limitation, possibly amplified by spreading anoxia or sulfide poisoning, would have preferentially wiped out the non-motile and physiologically unbuffered taxa[43]. Together, the distinct stressors led to a physiological crisis accompanied by a dramatic shrinking of the habitable realm, which limited the marine refuge to a narrow zone in the upper water column[24,47].

Given the vastly differing timescales and carbon budgets involved, LIP carbon cycle dynamics is a poor analogy for present-day fossil fuel emissions; notwithstanding that, the modern geological carbon reservoirs are insufficient for anthropogenic release beyond centennial time scales. It is, however, noteworthy that even the peak emissions rate during the largest known mass extinction (58×10^{12} mol CO_2 or 0.7 Pg C per year) is still more than 14 times less than the current anthropogenic rate (9.9 ± 0.5 Pg C per year)[48]. The environmental deterioration during the PTB took several thousands of years to unfold, whereas the current, unprecedented emissions rate has already started to take a toll on the marine ecosystems[49]. A coupled increase in atmospheric p_{CO_2} and decrease in surface ocean pH[49], global warming, changes in productivity and oxygen depletion[50] have been reported worldwide, which suggests that the scenario outlined here for the PTB may also be relevant to understanding future environmental and climatic trends.

Online content

Any methods, additional references, Nature Research reporting summaries, source data, extended data, supplementary information, acknowledgements, peer review information; details of author contributions and competing interests; and statements of data and code availability are available at https://doi.org/10.1038/s41561-020-00646-4.

Received: 22 August 2018; Accepted: 14 September 2020;
Published online: 19 October 2020

References

1. Burgess, S. D., Bowring, S. & Shen, S.-Z. High-precision timeline for Earth's most severe extinction. *Proc. Natl Acad. Sci. USA* **111**, 3316–3321 (2014).
2. Svensen, H. et al. Siberian gas venting and the end-Permian environmental crisis. *Earth Planet. Sci. Lett.* **277**, 490–500 (2009).
3. Burgess, S. D. & Bowring, S. A. High-precision geochronology confirms voluminous magmatism before, during, and after Earth's most severe extinction. *Sci. Adv.* **1**, e1500470 (2015).
4. Saunders, A. D. Two LIPs and two Earth-system crises: the impact of the North Atlantic igneous province and the Siberian Traps on the Earth-surface carbon cycle. *Geol. Mag.* **153**, 201–222 (2016).
5. Cui, Y. & Kump, L. R. Global warming and the end-Permian extinction event: proxy and modeling perspectives. *Earth Sci. Rev.* **149**, 5–22 (2015).
6. Sun, Y. et al. Lethally hot temperatures during the early Triassic greenhouse. *Science* **338**, 366–370 (2012).
7. Brand, U. et al. The end-Permian mass extinction: a rapid volcanic CO_2 and CH_4-climatic catastrophe. *Chem. Geol.* **323**, 121–144 (2012).
8. Winguth, A. M. E., Shields, C. A. & Winguth, C. Transition into a hothouse world at the Permian–Triassic boundary—a model study. *Palaeogeogr. Palaeoclimatol. Palaeoecol.* **440**, 316–327 (2015).
9. Garbelli, C. et al. Neotethys seawater chemistry and temperature at the dawn of the end-Permian mass extinction. *Gondwana Res.* **35**, 272–272 (2016).
10. Wang, W. et al. A high-resolution middle to late Permian paleotemperature curve reconstructed using oxygen isotopes of well-preserved brachiopod shells. *Earth Planet. Sci. Lett.* **540**, 116245 (2020).
11. Lau, K. V. et al. Marine anoxia and delayed Earth system recovery after the end-Permian extinction. *Proc. Natl Acad. Sci. USA* **113**, 2360–2365 (2016).
12. Elrick, M. et al. Global-ocean redox variation during the middle-late Permian through Early Triassic based on uranium isotope and Th/U trends of marine carbonates. *Geology* **45**, 163–166 (2017).
13. Zhang, F. F. et al. Congruent Permian–Triassic $\delta^{238}U$ records at Panthalassic and Tethyan sites: confirmation of global-oceanic anoxia and validation of the U-isotope paleoredox proxy. *Geology* **46**, 327–330 (2018).
14. Korte, C. et al. Carbon, sulfur, oxygen and strontium isotope records, organic geochemistry and biostratigraphy across the Permian/Triassic boundary in Abadeh, Iran. *Int. J. Earth Sci.* **93**, 565–581 (2004).
15. Grice, K. et al. Photic zone euxinia during the Permian–Triassic superanoxic event. *Science* **307**, 706–709 (2005).
16. Payne, J. L. et al. Calcium isotope constraints on the end-Permian mass extinction. *Proc. Natl Acad. Sci. USA* **107**, 8543–8548 (2010).
17. Clarkson, M. O. et al. Ocean acidification and the Permo-Triassic mass extinction. *Science* **348**, 229–232 (2015).
18. Garbelli, C., Angiolini, L. & Shen, S.-Z. Biomineralization and global change: a new perspective for understanding the end-Permian extinction. *Geology* **45**, 19–22 (2017).
19. Hönisch, B., Hemming, N. G., Archer, D., Siddall, M. & McManus, J. F. Atmospheric carbon dioxide concentration across the mid-Pleistocene transition. *Science* **324**, 1551–1554 (2009).
20. Rae, J. W. B. et al. CO_2 storage and release in the deep Southern Ocean on millennial to centennial timescales. *Nature* **562**, 569–573 (2018).
21. Gutjahr, M. et al. Very larger release of mostly volcanic carbon during the Palaeocene–Eocene thermal maximum. *Nature* **548**, 573–577 (2017).
22. Henehan, M. et al. Rapid ocean acidification and protracted Earth system recovery followed the end-Cretaceous Chicxulub impact. *Proc. Natl Acad. Sci. USA* **116**, 22500–22504 (2019).
23. Müller, T. et al. Ocean acidification during the early Toarcian extinction event: Evidence from boron isotopes in brachiopods. *Geology* https://doi.org/10.1130/G47781.1 (2020).
24. Posenato, R. Survival patterns of microbenthic marine assemblages during the end-Permian mass extinction in the western Tethys (Dolomites, Italy). *Palaeogeogr. Palaeoclimatol. Palaeoecol.* **280**, 150–167 (2019).
25. Wallmann, K. et al. Periodic changes in the Cretaceous ocean and climate caused by marine redox see-saw. *Nat. Geosci.* **12**, 456–462 (2019).
26. Retallack, G. J. A 300-million-year record of atmospheric carbon dioxide from fossil plant cuticles. *Nature* **411**, 287–290 (2001).
27. Goddéris, Y. et al. Causal or casual link between the rise of nannoplankton calcification and a tectonically-driven massive decrease in Late Triassic atmospheric CO_2? *Earth Planet. Sci. Lett.* **267**, 247–255 (2008).
28. McElwain, J. C., Wagner, P. J. & Hesselbo, S. P. Fossil plant relative abundances indicate sudden loss of Late Triassic biodiversity in East Greenland. *Science* **324**, 1554–1556 (2009).
29. Witkowski, C. R., Weijers, J. W. H., Blais, B., Schouten, S. & Damste, J. S. S. Molecular fossils from phytoplankton reveal secular p_{CO_2} trend over the Phanerozoic. *Sci. Adv.* **4**, eaat4556 (2018).
30. Joachimski, M. M. et al. Climate warming in the latest Permian and the Permian–Triassic mass extinction. *Geology* **40**, 195–198 (2012).

31. Schobben, M., Joachimski, M. M., Korn, D., Leda, L. & Korte, C. Palaeotethys seawater temperature rise and an intensified hydrological cycle following the end-Permian mass extinction. *Gondwana Res.* **26**, 675–683 (2014).
32. Algeo, T. J. et al. Plankton and productivity during the Permian–Triassic boundary crisis: an analysis of organic carbon fluxes. *Glob. Planet. Change* **105**, 52–67 (2013).
33. Saitoh, M. et al. Nitrogen isotope chemostratigraphy across the Permian–Triassic boundary at Chaotian, Sichuan, South China. *J. Asian Earth Sci.* **93**, 113–128 (2014).
34. Sun, Y. D. et al. Ammonium ocean following the end-Permian mass extinction. *Earth Planet. Sci. Lett.* **518**, 211–222 (2019).
35. Shen, J. et al. Marine productivity changes during the end-Permian crisis and Early Triassic recovery. *Earth Sci. Rev.* **149**, 136–162 (2015).
36. Canfield, D. E. Models of oxic respiration, denitrification and sulfate reduction in zones of coastal upwelling. *Geochim. Cosmochim. Acta* **70**, 5753–5765 (2006).
37. Anderson, R. F. et al. Deep-sea oxygen depletion and ocean carbon sequestration during the last ice age. *Glob. Biogeochem. Cycles* **33**, 301–317 (2019).
38. Zeebe, R. & Westbroek, P. A simple model for the $CaCO_3$ saturation state of the ocean: The 'Strangelove', the 'Neritan', and the 'Cretan' Ocean. *Geochem. Geophys. Geosyst.* **4**, 1104 (2003).
39. Vollstaedt, H. et al. The Phanerozoic $\delta^{88/86}$Sr record of seawater: new constraints on past changes in oceanic carbonate fluxes. *Geochim. Cosmochim. Acta* **128**, 249–265 (2014).
40. Silva-Tamayo, J. C. et al. Global perturbation of the marine calcium cycle during the Permian–Triassic transition. *Geol. Soc. Am. Bull.* **130**, 1323–1338 (2018).
41. Woods, A. Assessing Early Triassic paleoceanographic conditions via unusual sedimentary fabrics and features. *Earth Sci. Rev.* **137**, 6–18 (2014).
42. Burgess, S. D., Muirhead, J. D. & Bowring, S. A. Initial pulse of Siberian Traps sills as the trigger of the end-Permian mass extinction. *Nat. Commun.* **8**, 164 (2017).
43. Song, H. J., Wignall, P. B., Tong, J. N. & Yin, H. F. Two pulses of extinction during the Permian–Triassic crisis. *Nat. Geosci.* **6**, 52–56 (2013).
44. Brayard, A. et al. Transient metazoan reefs in the aftermath of the end-Permian mass extinction. *Nat. Geosci.* **4**, 693–697 (2011).
45. Martindale, R. C., Foster, W. J. & Velledits, F. The survival, recovery, and diversification of Metazoan reef ecosystems following the end-Permian mass extinction event. *Palaeogeogr. Palaeoclimatol. Palaeoecol.* **513**, 100–115 (2019).
46. Reynard, S. et al. Interacting effects of CO2 partial pressure and temperature on photosynthesis and calcification in a scleractinian coral. *Glob. Change Biol.* **9**, 1660–1668 (2003).
47. Beatty, T. W., Zonneveld, J.-P. & Henderson, C. M. Anomalously diverse Early Triassic ichnofossil assemblages in northwest Pangea: a case for shallow-marine habitable zone. *Geology* **36**, 771–774 (2008).
48. Le Quéré, C. et al. Global carbon budget 2018. *Earth Syst. Sci. Data* **10**, 2141–2194 (2018).
49. Orr, J. C. et al. Anthropogenic ocean acidification over the twenty-first century and its impact on calcifying organisms. *Nature* **437**, 681–686 (2005).
50. Schmidtko, S., Stramma, L. & Visbeck, M. Decline in global oxygen content during the past five decades. *Nature* **542**, 335–339 (2017).

Methods

Site and sample information. We selected fossil brachiopods from well-constrained successions of the eastern Southern Alps (Sass de Putia, Tesero and Val Brutta in Italy; see Posenato[51] for an overview) and Shangsi (China)[18] that spanned the PTB interval. We opted for this novel archive approach for two particular reasons; first, because skeletal components of marine calcifiers are the most appropriate boron-based pH recorders[19–23] and, second, because brachiopod shells are composed of low-magnesium calcite, the most robust polymorph of calcium carbonate to diagenetic alterations. Our records are based on carefully chosen unaltered specimens from a collection[7] that was extensively prescreened with optical and petrographic inspections, scanning electron microscopy (Supplementary Information), cathodoluminescence and polarizing microscopy alongside criteria based on trace, rare earth and redox-sensitive elements to assure microstructural and chemical integrity. Additionally, further related specimens from the collections of R.P. and L.A. were used to complement the set, which allowed us to extend the timeline and the resolution of the previous records, and capture the full span of the $\delta^{13}C$ excursion. Brachiopods from these PTB sections are extremely well preserved with discernible internal layers analogous to that in modern brachiopods[7,52–54]. The brachiopod taxa from the Southern Alps comprise the genera *Comelicania*, *Comelicothyris*, *Janiceps* and *Orbicoelia* of the class Rhynchonellata, and *Ombonia*, *Orthothetina* and *Teserina* of the class Strophomenata. To evaluate whether the pH suppression observed in our record from the Southern Alps was a Tethys-wide event, we also included selected *Paracrurithyris* (Rhynchonellata) specimens from the Shangsi section[18] in the record for a comparison. The age model was based on a stratigraphic correlation to the Meishan GSSP and the latest absolute geochronologic dates[1]. Further description of the stratigraphy and our devised age model is available in the Supplementary Section 1. The palaeogeographic map reconstruction, including the extent of the Siberian Traps province, was based on geological evidence[55,56].

Sample preparation and geochemical analyses. The inner secondary layer of brachiopod shells is deemed as the most appropriate part for geochemical analyses[57,58] and was carefully sampled using a handheld precision drill (Proxxon) with a mounted dental tip or a carbide pen under a binocular microscope. Approximately 1–5 mg of homogeneous calcium carbonate powder was collected in 1.5 ml centrifuge vials. A small fraction of the powder was analysed for $\delta^{13}C$ and $\delta^{18}O$ composition on a Thermo Finnigan MAT252 isotope ratio mass spectrometer (IRMS) coupled online to an automated Kiel carbonate preparation line. The rest was measured for elemental content and $\delta^{11}B$ using inductively coupled plasma mass spectrometry (ICP-MS) on an Agilent 7500 quadrupole ICP-MS and a Thermo Scientific Neptune Plus multicollector (MC) ICP-MS, respectively. Measurements and sample preparation work was carried out at the GEOMAR Helmholtz Centre for Ocean Research Kiel. Purification and the treatment of the samples for elemental and $\delta^{11}B$ analyses were carried out according to previously established protocols[59,60]. The powder material was at first thoroughly cleaned to remove any adhering clays, then oxidatively cleaned using buffered peroxide and finally dissolved in 0.5 M HNO_3. Prior to $\delta^{11}B$ analyses, samples were additionally screened for structural preservation (section 2 of the Supplementary Information), and chemical consistency by checking various elemental ratios (Al/Ca, B/Ca, Mg/Ca, Sr/Ca, Mn/Ca, Fe/Ca and U/Ca; Extended Data Fig. 1). Although few samples had elevated Al/Ca, similar to observations from previous studies[21,23], this did not translate into altered $\delta^{11}B$ values, as supported by the good agreement between solution-based and in situ SIMS measurements. Likewise, we observed variable B/Ca, Mg/Ca, Sr/Ca, Mn/Ca, Fe/Ca and U/Ca; however, with the exception of a few samples, the measured values were within the range of recent brachiopods[57] and without a significant systematic effect on the $\delta^{11}B$ values. We also underline that, for the most part, our record is based on several specimens per stratigraphic horizon, with good agreement in $\delta^{11}B$ values between them despite variable Al/Ca or other ratios, which implies that any potential source of contamination to the samples had a limited impact on the $\delta^{11}B$ values. This is also supported by the very depleted B/Ca, but elevated and variable Al/Ca of the enclosing matrix based on three samples of Late Permian cement (Extended Data Fig. 1), which was the likely source. Ultimately though, as mentioned in the main text, our overall $\delta^{11}B$ trends may still be reconstructed when samples with low Al/Ca only are taken into account. Our total procedural blanks were below <100 pg B ($\delta^{11}B$ ~0–20‰) and hence negligible given the typical sample size of 10–50 ng B. The external reproducibility on $\delta^{11}B$ was ±0.2‰ (2 s.d.) assessed by repeated measurements of purified carbonate reference materials measured along with the samples and treated identically ($\delta^{11}B = 24.51 \pm 0.18$‰, $n = 5$ for the coral reference material JCp-1, and $\delta^{11}B = 15.96 \pm 0.21$‰, $n = 16$ for our in-house brachiopod standard MVS-1), in line with our previously published results[59]. In addition, in situ boron isotope measurements were carried out on selected key specimens using SIMS. This approach allowed for the determination of $\delta^{11}B$ values in brachiopod shells directly, without the chemical processing of samples, and with measured isotopic ratios being directly comparable to the solution-based MC-ICP-MS technique[59,61]. SIMS analyses and sample preparation was done at the GFZ German Research Centre for Geosciences—Helmholtz Centre Potsdam. Measurements were performed on a CAMECA 1280-HR SIMS instrument as described in detail in Supplementary Section 3. In brief, cross-sections of brachiopod shells were embedded in epoxy, and polished and coated with gold. We used a $^{16}O^-$ primary beam operated in Köhler illumination with the intensity varying between approximately 40 and 60 nA and focused into an aperture delimited spot of ~30 µm. The analyses were conducted in a multicollection mode by simultaneously measuring ^{10}B and ^{11}B on electron multipliers. For instrument calibration and the reporting of measured isotopic ratios to the common NIST 951 scale, we used the inorganic calcite reference material UWC-1[62]. The count rate on the $^{11}B^+$ mass station on UWC-1 was typically in the range 5,000–10,000 ions s^{-1}, which translated to an uncertainty of ~1 to 1.5‰ (s.d.) for individual analyses (for the brachiopod samples, the count rate was usually at least double that of UWC-1). The external analytical repeatability on UWC-1 over 4 days of the measurement session was better than ±1.4‰ (s.d., $n = 82$). Results are shown as a mean of multiple ion spot measurements within a single specimen with the s.d. between them.

pH calculation. A prerequisite for the reconstruction of pH from $\delta^{11}B$ values of marine biogenic carbonates is the knowledge of the $\delta^{11}B$ composition of seawater ($\delta^{11}B_{sw}$). Boron in seawater is homogeneous with a residence time of approximately 11–20 Myr, and thus the $\delta^{11}B_{sw}$ needs to be constrained for the PTB. The $\delta^{11}B_{sw}$ composition of the modern ocean is 39.6‰, but it was proposed to have been lower in the past (~37‰ 60 million years ago)[63]. Permian $\delta^{11}B_{sw}$ values were previously calculated by modelling of the boron geochemical cycle, which suggested a $\delta^{11}B_{sw}$ of ~38‰ for the Early Permian (Late Sakmarian) and a $\delta^{11}B_{sw}$ of ~34‰ for the latest Permian, just prior to the PTB[64]. To provide a further constraint on the $\delta^{11}B_{sw}$, but not obviate previous estimates, we considered a range of values that effectively envelopes the possible $\delta^{11}B_{sw}$, yet allows for the full expression of the proxy. Assuming that boron is incorporated into brachiopod calcite following the inorganic borate ion fractionation[65] with negligible vital effects, the maximum integer $\delta^{11}B_{sw}$ that enables the calculation of pH from all our brachiopod $\delta^{11}B$ values within the dynamic range of the proxy is 38‰, with values ≥39‰ being beyond the sensitivity of the proxy at the lower pH spectrum. However, applying a brachiopod calibration that accounts for biological influence on the incorporation of boron[66], the highest feasible integer $\delta^{11}B_{sw}$ is 35‰ (similarly, values ≥36‰ are beyond the proxy range at the lower pH spectrum). A lower-end limit on the $\delta^{11}B_{sw}$ can be placed by tying our average pre-event brachiopod $\delta^{11}B$ (14 ± 0.5‰, 2 s.d., $n = 7$, based on the mean composition of brachiopods from beds wPK5 top, wPK6A and wPK6A base; note that the specimens from beds PK4 are not included due to less reliable constraints on their age (also see Supplementary Section 1)) to probable pre-event pH conditions and inversely derive the $\delta^{11}B_{sw}$. Given that the modern ocean mean pH is 8.1, and Late Permian was a high p_{CO_2} world, but the ocean did not contain a carbonate buffer due to the lack of pelagic carbonate producers, it is reasonable to assume that pre-event pH must have been lower than that of today. Assuming a mean pre-event pH of ~7.8, based on model-derived constraints of Late Permian pH for a 'Neritan' ocean[67], the $\delta^{11}B_{sw}$ values of ~38‰ and ~35‰ via borate ion fractionation and brachiopod calibration, respectively, may be calculated (in this case, higher pre-event pH values would result in lower $\delta^{11}B_{sw}$ estimates). The choice of the pre-event pH value, and hence $\delta^{11}B_{sw}$, can be further supported by additional runs of our geochemical box model when forced not to violate constraints given by LIP degassing and the global $\delta^{13}C$ record (Supplementary Section 4).

In addition to the $\delta^{11}B_{sw}$, the application of an appropriate archive-specific $\delta^{11}B$ calibration is required to calculate pH from $\delta^{11}B$ values. Typically, more recent reconstructions that span the Neogene employ extant archives (for example, foraminifera or corals), from which a pH-dependent $\delta^{11}B$ calibration can be made using culture or field studies to assess the role of vital effects due to their internal biological processes. This is, however, not possible for any Palaeozoic brachiopods, which are extinct and thus such assessments must be made indirectly. Similar to the calculation of $\delta^{11}B_{sw}$, to account for different influences on the incorporation of boron into brachiopod shells, we considered two different calibrations; the inorganic $\delta^{11}B$-to-pH relationship of the aqueous borate ion[65] and a brachiopod calibration that brackets their vital effects[66]. As vital effects are also undoubtedly inherent to brachiopods, as in other calcifiers, we chose the pH reconstruction based on brachiopod calibration[66] as our preferred scenario (standard case scenario). However, for comparison we also provide a second detailed scenario based on pH values calculated using the borate ion relationship (borate ion scenario; Extended Data Fig. 3 and detailed in Supplementary Section 4).

Two further calibrations are found in the literature; a calibration based on modern terebratellids[68] and a calibration based on cultured *Magellania venosa*[59]. The first one[68] results in pH estimates rather similar to that of the brachiopod calibration of Lécuyer et al.[66]. In comparison, the *M. venosa* calibration[59] results are highly sensitive within the defined $\delta^{11}B_{sw}$ envelope, with only minor $\delta^{11}B$ variations resulting in an extreme pH change, which are in most instances beyond the dynamic proxy range. A pH reconstruction is, nonetheless, feasible using the *M. venosa* calibration[59] if $\delta^{11}B_{sw} < 30$‰. Such low $\delta^{11}B_{sw}$ values, however, at present appear rather unlikely for the PTB. Hence, although the *M. venosa* calibration appears to be applicable to other recent cold-water species as well, we suspect that it is not suited for Palaeozoic brachiopods. Moreover, many modern terebratellids, and specifically *M. venosa*, thrive in highly dynamic cold-water regimes characteristic of large seasonal variations and, as a result, probably exhibit stronger vital effects than ancient warm-water dwelling species.

Species-specific vital effects may further complicate the use of one general calibration[68]. To overcome this, and because the use of multiple brachiopod species appears inevitable to provide a PTB record of sufficient temporal resolution, we considered the following measures. First, we strictly limited the number of species used in our record, but in particular brachiopod classes as brachiopods vary mostly at a higher taxonomic level[69]. Second, because vital effects are closely linked to an organism's niche, we examined the habitat and morphology parallels between the species used. Finally, we devised the record taking into account the stratigraphic overlap between the different species during the pre-event as well as the event conditions, which gives us confidence that the final reconstruction is not significantly affected by species-specific offsets. Indeed, the overall $\delta^{11}B$ trend of our full record holds when solely based on one brachiopod group (Rhynchonellata) from one site (Southern Alps, northern Italy; Extended Data Fig. 2).

The Late Permian record prior to the CIE is almost exclusively based on *Comelicania* spp., but also includes two specimens of *Janiceps* spp. (both Rhynchonellata), which show a close agreement, not larger than the typical intraspecific variations among different *Comelicania* spp. shells. Just after the CIE, the record still includes several *Comelicania* spp., but also few other species that belong to both Rhynchonellata and Strophomenata. Note that bed wPK11B (apparently 7 kyr relative to the CIE) comprises *Janiceps* spp. and *Comelicothyris* spp. (both Rhynchonellata) as well as *Ombonia* spp. (Strophomenata) specimens, which show highly similar $\delta^{11}B$ values (13.18 ± 0.48, s.d. between specimens, $n = 6$), which further supports the fact that interspecific variations, even at a class level, are minimal and do not significantly impact our $\delta^{11}B$ values. The latest part of our record that documents acidification, despite the scarcity of brachiopods in these beds, is based on both brachiopod classes with multiple specimens of *Orbicoelia* spp. (Rhynchonellata) and *Teserina* spp. (Strophomenata) from northern Italy, as well as *Paracrurithyris* spp. (Rhynchonellata) from South China, which offer firm evidence for the pH trends presented in this study.

The effect of the dissociation constant for boric acid (pK_B^*) on the calculated pH is comparatively only very minor. For our pH calculation, we used $pK_B^* = 8.60$, which corresponds to the typical pre-event temperatures of about 25 °C and salinity of 35, based on our data as well as on conodont-derived pre-event temperatures[6,30] and considering that the general Late Permian salinity[31,70] and major ion chemistry and mineralogy[71] was largely similar to present-day conditions. We note that a temperature increase by 5 or 10 °C, for example, would give a pK_B^* of 8.54 or 8.48, which would translate to a decrease in pH values by 0.06 and 0.12 units, respectively. This would only magnify the reported pH decline simultaneous with the major phase of warming, although at such a low pH range the pK_B^* influences on pH values would be largely within the uncertainties.

Model setup. A geochemical box model was set up to simulate the processes in the global ocean based on a recent ocean circulation model[8] for the PTB (see Supplementary Section 4 for a detailed description of the model). Basin volumes, seafloor areas and the water fluxes between the boxes employed in the model are taken from the circulation model (Extended Data Fig. 5). The recently developed redox-resolving biogeochemistry model REDBIO[25] was coupled to the box model to simulate the biogeochemical turnover in the ocean. REDBIO considers the following dissolved tracers: oxygen, nitrate, ammonium, phosphate, ferric iron, ferrous iron, total dissolved sulfide, dissolved inorganic carbon (^{12}C and ^{13}C) and total alkalinity. All the tracer inventories change over time due to weathering inputs from land, CO_2 and O_2 fluxes across the ocean–atmosphere interface, nitrogen fixation, denitrification and redox-dependent fluxes at the seabed. Continental weathering and degassing fluxes, surface temperatures and atmospheric p_{CO_2} were simulated using the GEOCARB process formulations[72,73], whereas marine $\delta^{13}C$ values were calculated as described in a previous box model[74]. REDBIO was further extended to simulate the turnover of stable nitrogen isotopes in the ocean, considering the total concentrations of dissolved nitrate and ammonium as well as the concentrations of ^{15}N nitrate and ^{15}N ammonium.

The model was run for a period of 2 Myr to reach a Late Permian equilibrium. Subsequently, a pulse of volcanic/metamorphic CO_2 was released to study the consequences of LIP degassing. The boundary parameters, which included the equilibrium climate sensitivity of 3 °C per doubling of p_{CO_2}, were chosen based on the GEOCARB[75] models. Model results are shown on a timescale in which the zero point is set at the onset of the negative CIE. The CO_2 flux induced by LIP degassing and its isotopic composition were varied systematically until the $\delta^{13}C$ of carbonates deposited on the continental shelf of the Tethys Ocean (see Supplementary Section 4 for data sources) and the pH values in the Tethys surface water were consistent with the available data (Fig. 2). Comparison of our model-derived atmospheric p_{CO_2} with previously published estimates[5] based on stomatal indices is available in Supplementary Section 5. Throughout the manuscript we use the terminology Tethys Ocean, which combines both Neotethys and Palaeotethys Oceans, as they are represented by a common box in the model.

Data availability

We have chosen not to deposit the data in a repository at this time, but all the geochemical data analysed during this study are accessible in the Supplementary Data file.

Code availability

Computer code is available upon reasonable request from K.W. (kwallmann@geomar.de).

References

51. Posenato, R. Marine biotic events in the Lopingian succession and latest Permian extinction in the Southern Alps (Italy). *Geol. J.* **45**, 195–215 (2010).
52. Broglio Loriga, C., Neri, C., Pasini, M. & Posenato, R. in *Permian and Permian–Triassic Boundary in the South-Alpine segment of the western Tethys, and Additional Reports* (ed. Cassinis, G.) 5–44 (Societa Geologica Italiana, 1988).
53. Posenato, R. The athyridoids of the transitional beds between Bellerophon and Werfen formations (uppermost Permian, Southern Alps, Italy). *Riv. Ital. Paleontol. Soc.* **1071**, 197–226 (2001).
54. Kearsey, T., Twichett, R. J., Price, G. D. & Grimes, S. T. Isotope excursion and palaeotemperature estimates from the Permian/Triassic boundary in the Southern Alps (Italy). *Palaeogeogr. Palaeoclimatol. Palaeoecol.* **279**, 29–40 (2009).
55. Muttoni, G. et al. Opening of the neo-Tethys ocean and the Pangea B to Pangea A transformation during the Permian. *GeoArabia* **14**, 17–48 (2009).
56. Reichow, M. K. et al. The timing and extent of the eruption of the Siberian Traps large igneous province: implications for the end-Permian environmental crisis. *Earth Planet. Sci. Lett.* **277**, 9–20 (2009).
57. Brand, U., Logan, A., Hiller, N. & Richardson, J. Geochemistry of modern brachiopods: applications and implications for oceanography and paleoceanography. *Chem. Geol.* **198**, 305–334 (2003).
58. Rollion-Bard, C. et al. Assessing the biomineralisation processes in the shell layers of modern brachiopods from oxygen isotopic composition and elemental ratios: implications for their use as paleoenvironmental proxies. *Chem. Geol.* **524**, 49–66 (2019).
59. Jurikova, H. et al. Boron isotope systematics of cultured brachiopods: response to acidification, vital effects and implications for palaeo-pH reconstruction. *Geochim. Cosmochim. Acta* **248**, 370–386 (2019).
60. Jurikova, H. et al. Incorporation of minor and trace elements into cultured brachiopods: implications for proxy application with new insights from a biomineralisation model. *Geochim. Cosmochim. Acta* **286**, 418–440 (2020).
61. Jurikova, H. et al. Boron isotope composition of the cold-water coral *Lophelia pertusa* along the Norwegian margin: zooming into a potential pH-proxy by combining bulk and high-resolution approaches. *Chem. Geol.* **513**, 143–152 (2019).
62. Kasemann, S. A., Schmidt, D. N., Bijima, J. & Foster, G. L. *In situ* boron isotope analyses in marine carbonates and its application for foraminifera and palaeo-pH. *Chem. Geol.* **260**, 138–147 (2009).
63. Lemarchand, D., Gaillardet, J., Lewin, É. & Allègre, C. J. The influence of rivers on marine boron isotopes and implications for reconstructing past ocean pH. *Nature* **408**, 951–954 (2000).
64. Joachimski, M. M., Simon, L., van Geldern, R. & Lécuyer, C. Boron isotope geochemistry of Paleozoic brachiopod calcite: implications for a secular change in the boron isotope geochemistry of seawater over the Phanerozoic. *Geochim. Cosmochim. Acta* **69**, 4035–4044 (2005).
65. Klochko, K., Kaufman, A. J., Wengsheng, Y., Byrne, R. H. & Tossell, J. A. Experimental measurement of boron isotope fractionation in seawater. *Earth Planet. Sci. Lett.* **248**, 276–285 (2006).
66. Lécuyer, C., Grandjean, P., Reynard, B., Albarède, F. & Telouk, P. $^{11}B/^{10}B$ analysis of geological materials by ICP-MS Plasma 54: application to the boron fractionation between brachiopod calcite and seawater. *Chem. Geol.* **186**, 45–55 (2002).
67. Ridgwell, A. A mid Mesozoic revolution in the regulation of ocean chemistry. *Mar. Chem.* **217**, 339–357 (2005).
68. Penman, D. E., Hönisch, B., Rasbury, E. T., Hemming, N. G. & Spero, H. J. Boron, carbon, and oxygen isotopic composition of brachiopod shells: intra-shell variability, controls, and potential as a paleo-pH recorder. *Chem. Geol.* **340**, 32–39 (2013).
69. Garbelli, C., Angiolini, L., Brand, U. & Jadoul, F. Brachiopod fabric, classes and biogeochemistry: implications for the reconstruction and interpretation of seawater carbon-isotope curves and records. *Chem. Geol.* **371**, 60–67 (2014).
70. Khiel, J. T. & Shields, C. A. Climate simulations of the latest Permian: implications for mass extinction. *Geology* **33**, 757–760 (2005).
71. Lowenstein, T. K., Timofeeff, M. N., Brennan, S. T., Hardie, L. A. & Demicco, R. V. Oscillations in Phanerozoic seawater chemistry: evidence from fluid inclusions. *Science* **294**, 1086–1088 (2001).
72. Berner, R. A. & Kothavala, Z. GEOCARB III: A revised model of atmospheric CO_2 over Phanerozoic time. *Am. J. Sci.* **301**, 182–204 (2001).
73. Royer, D. L., Donnadieu, Y., Park, J., Kowalczyk, J. & Godderis, Y. Error analysis of CO_2 and O_2 estimates from the long-term geochemical model GEOCARBSULF. *Am. J. Sci.* **314**, 1259–1283 (2014).

74. Wallmann, K., Schneider, B. & Sarnthein, M. Effects of eustatic sea-level change, ocean dynamics, and nutrient utilization on atmospheric p_{CO_2} and seawater composition over the last 130,000 years. *Clim. Past* **12**, 339–375 (2016).
75. Berner, R. A. GEOCARB II: a revised model of atmospheric CO_2 over Phanerozoic time. *Am. J. Sci.* **294**, 56–91 (1994).

Acknowledgements

This project has received funding from the European Union's Horizon 2020 research and innovation programme under the Marie Sklodowska-Curie grant agreement no. 643084 (BASE-LiNE Earth). K.W. was supported by the HGF (ESM project) and S.F. by the DFG (SFB 754, subproject A7). L.A. and R.P. were supported by the MURST (PRIN 2017RX9XXXY, project 'Biota resilience to global change: biomineralization of planktic and benthic calcifiers in the past, present and future'). We thank D. Nürnberg for help with the carbon and oxygen isotope analyses, and A. Kolevica and T. Goepfert for laboratory support (at the GEOMAR Helmholtz Centre for Ocean Research in Kiel). We are grateful to F. Couffignal and A. Rocholl for assistance with the SIMS analyses, U. Dittmann for sample preparation and I. Schäpan for scanning electron microscopy imaging (at the GFZ German Research Centre for Geosciences—Helmholtz Centre Potsdam). Special thanks to A. Winguth (at the University of Texas Arlington) for providing us the model output.

Author contributions

H.J., M.G., V.L. and A.E. developed the concept and designed the study. H.J. carried out the chemical sample preparation, as well as elemental and isotopic analyses. M.W. provided isotopic microanalyses. U.B., R.P., L.A. and C.G. provided and screened the samples. R.P., L.A., C.G. and H.J. developed the age model. K.W. and S.F. devised the box model and performed the analyses. H.J. wrote the manuscript, and all the authors discussed the results, contributed to the interpretation of the data and to the final manuscript.

Competing interests

The authors declare no competing interests.

Additional information

Extended data is available for this paper at https://doi.org/10.1038/s41561-020-00646-4.

Supplementary information is available for this paper at https://doi.org/10.1038/s41561-020-00646-4.

Correspondence and requests for materials should be addressed to H.J.

Peer review information Primary Handling Editor: Rebecca Neely.

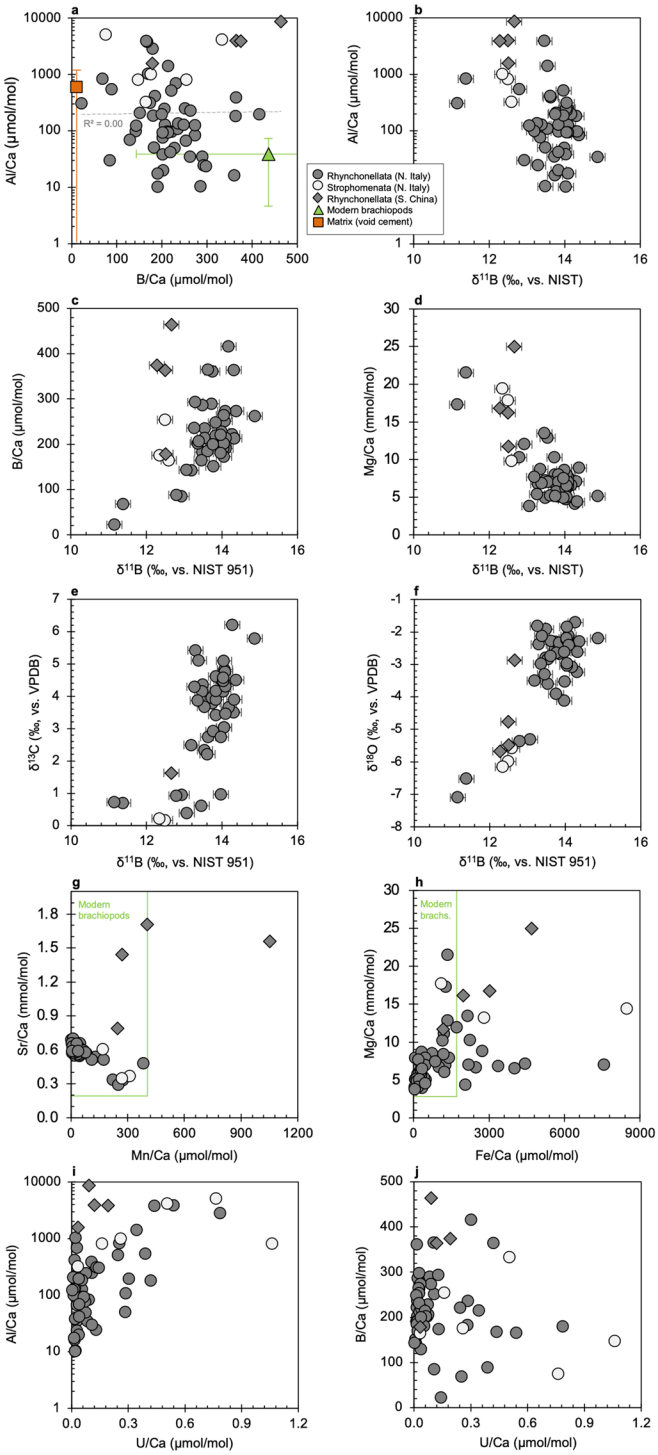

Extended Data Fig. 1 | Stable isotope and Element-to-Ca ratio cross-plots for PTB brachiopods. Grey symbols show data from solution-based analyses of PTB brachiopods. Panel **a** additionally shows the Al/Ca and B/Ca composition of matrix (void cement) material (n = 3, ±2 s.d.) and modern brachiopods (n = 3, ±2 s.d.; based on measured values for *Magellania venosa*, *Liothyrella neozelandica* and *Pajaudina atlantica*) for comparison. Matrix is highly depleted in B/Ca, with variable Al/Ca. Recent brachiopods are highly variable in both B/Ca and Al/Ca. Elemental ranges (Sr, Mn, Mg and Fe) for modern brachiopods shown in panels **g** and **h** are based on data from ref. [57].

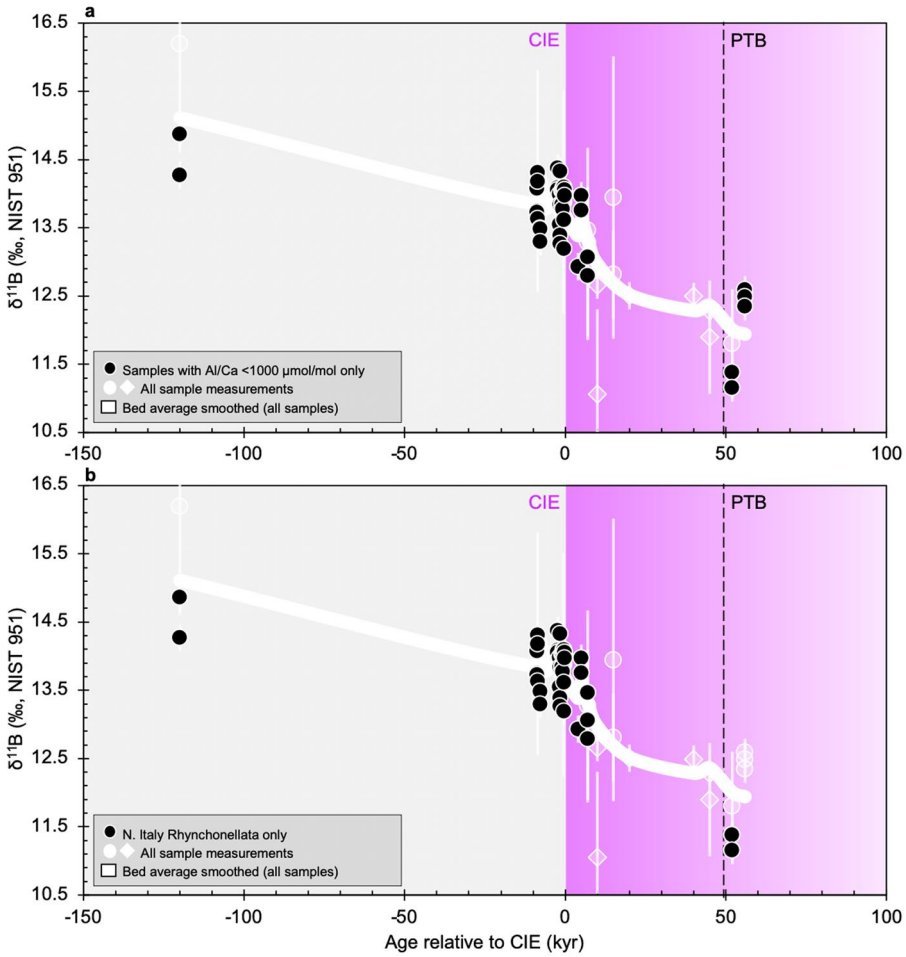

Extended Data Fig. 2 | Criteria-based boron isotope record shown relative to carbon isotope excursion (CIE; in kyr). a Boron isotope trends when solely based on samples with low Al/Ca ratios (Al/Ca <1000 µmol/mol); **b** boron isotope trends when solely based on one brachiopod class (Rhynchonellata) from one site (Southern Alps, northern Italy).

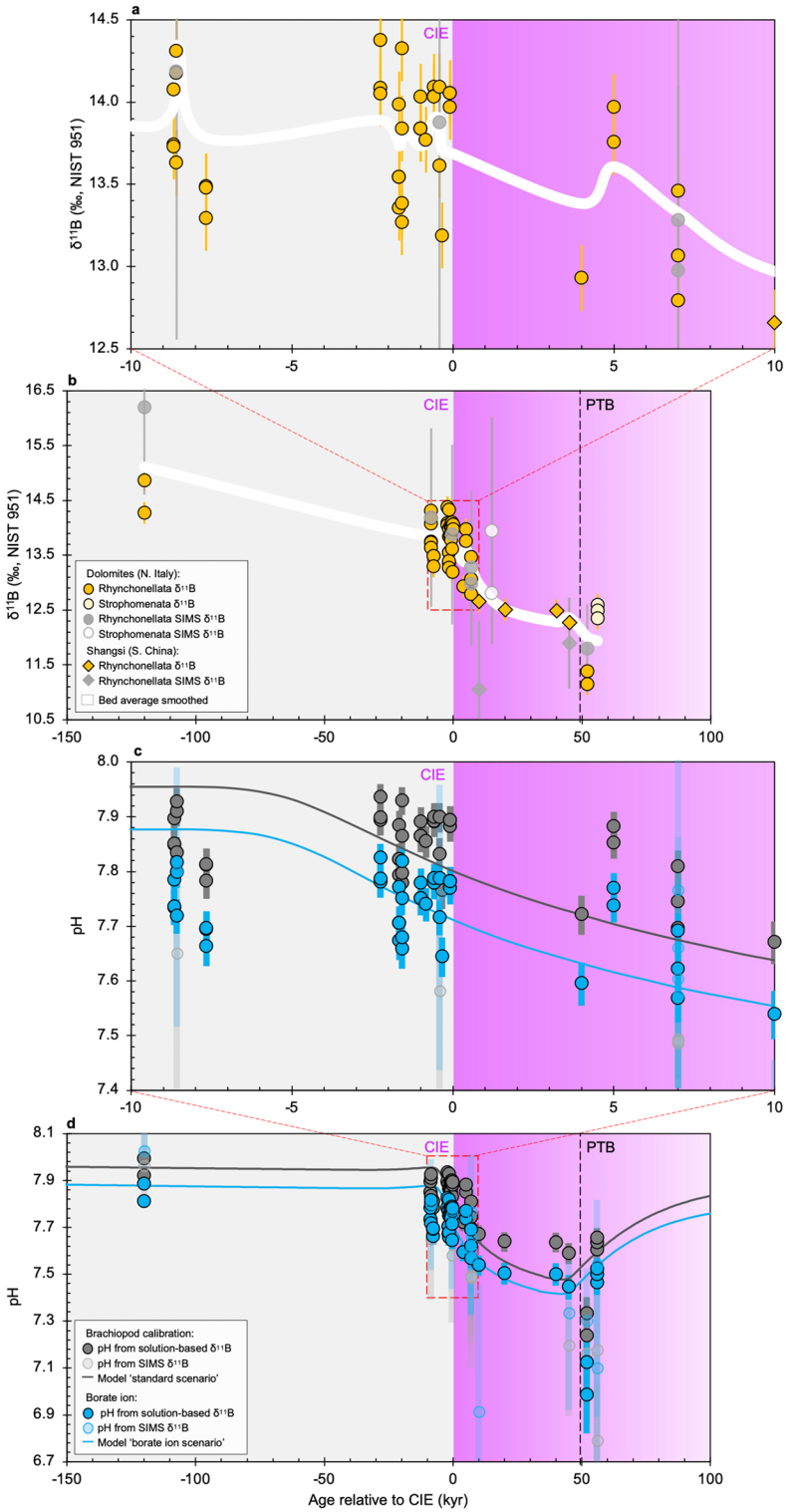

Extended Data Fig. 3 | Boron isotope and pH record shown relative to carbon isotope excursion (CIE; in kyr). Red dashed rectangle in panels **b** and **d** indicates the enlarged areas shown in **a** and **c**, respectively. Boron-derived pH values (**c**, **d**) are provided for each data point together with best fit model curve. Our preferred standard case scenario (in grey) is shown along with an alternative borate ion scenario (in blue) for comparison. Error bars for solution-based $\delta^{11}B$ values indicate the analytical uncertainty (2 s.d. = 0.2 ‰) and for SIMS $\delta^{11}B$ the s.d. between multiple ion spots measurements within a single sample (panels **a**, **b**). Error bars for pH are based on the given $\delta^{11}B$ envelope.

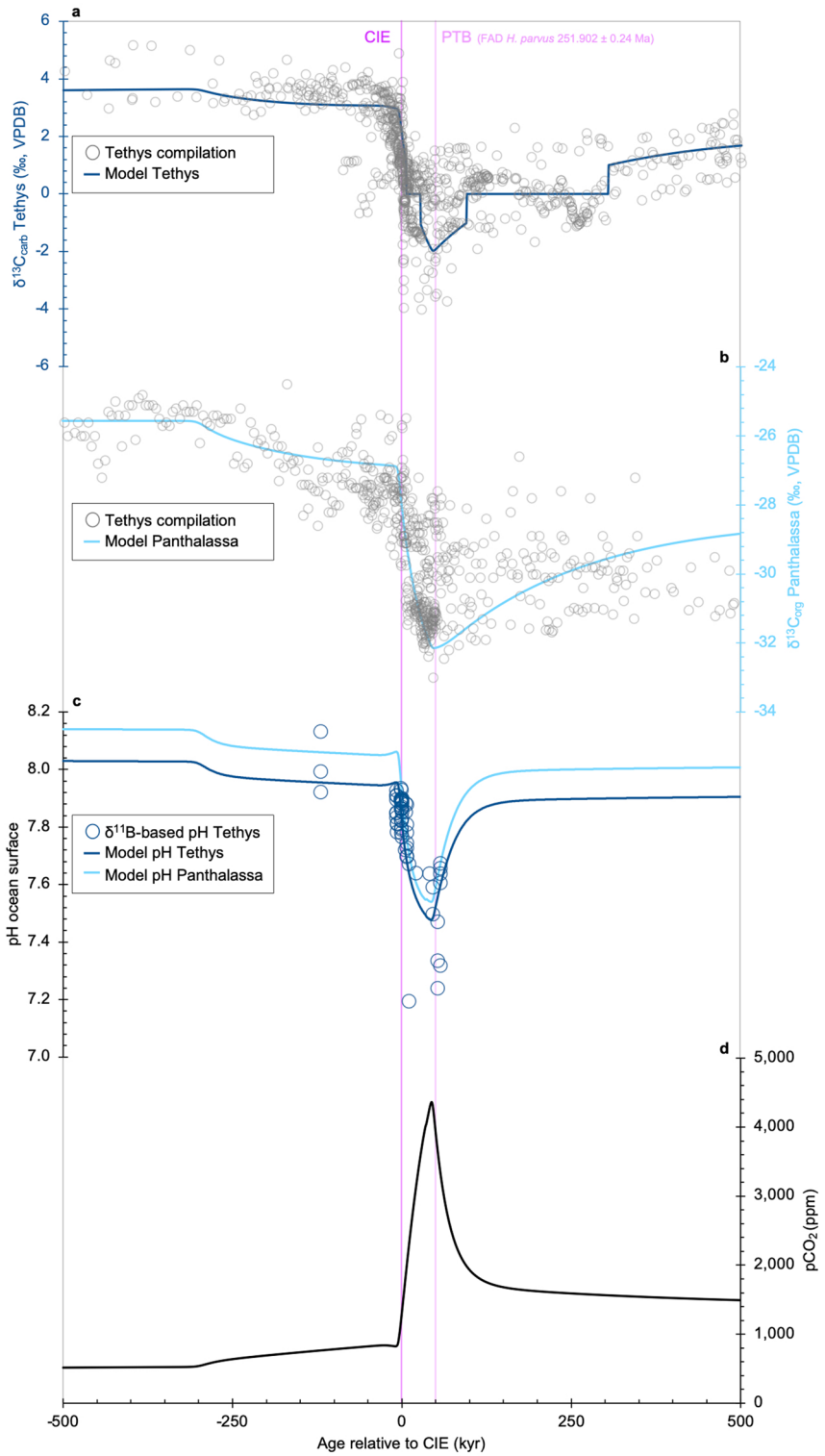

Extended Data Fig. 4 | Isotopic and model-based constraints on carbon cycle dynamics across the PTB. a Carbon isotope composition of carbonates deposited on Tethys shelf; and **b** carbon isotope composition of organic carbon in sediments deposited on Panthalassa seafloor based on a comprehensive compilation of literature data (sources are provided in the Supplement) and as modelled; **c** δ^{11}B-based and modelled surface ocean pH (standard case scenario); **d** resulting global atmospheric partial pressure CO_2 projected by our carbon cycle model.

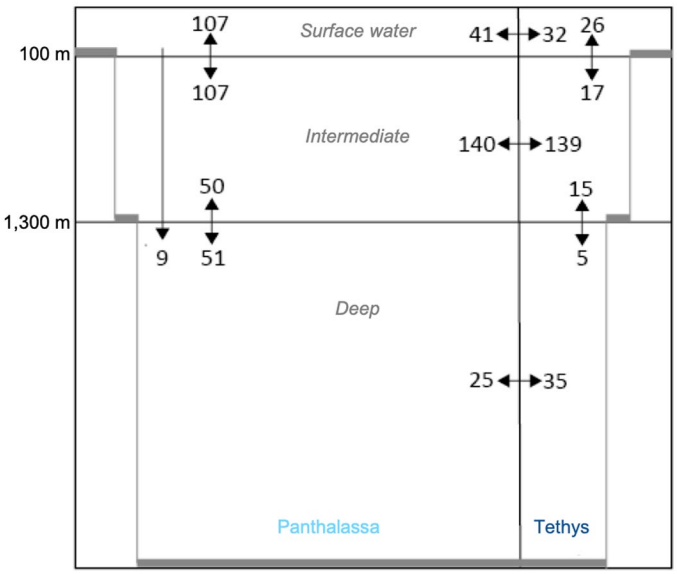

Extended Data Fig. 5 | Our box model setup. The global ocean is represented by 6 boxes: surface water (0–100 m water depth), intermediate water (100–1,300 m), and deep water (>1,300) for both, Tethys and Panthalassa oceans. Water fluxes across the box boundaries are given in Sv.